Topologically compatible non-Hermitian skin effect

Rijia Lin and Linhu Li [*]

*Guangdong Provincial Key Laboratory of Quantum Metrology and Sensing & School of Physics and Astronomy,
Sun Yat-Sen University (Zhuhai Campus), Zhuhai 519082, China*

The bulk-boundary correspondence (BBC) relates in-gap boundary modes to bulk topological invariants. In certain non-Hermitian topological systems, conventional BBC becomes invalid in the presence of the non-Hermitian skin effect (NHSE), which manifests as distinct energy spectra under the periodic and open boundary conditions and massive eigenstate localization at boundaries. In this paper, we introduce a scheme to induce NHSE without breaking conventional BBC, dubbed as the topologically compatible NHSE (TC-NHSE). In a general one-dimensional two-band model, we unveil two types of TC-NHSE that do not alter topological phase transition points under any circumstance or only in a certain parameter regime, respectively. Extending our model into two dimension, we find that TC-NHSE can be selectively compatible to different sets of Weyl points between different bands of the resultant semimetallic system, transforming some of them exceptional points connected by bulk Fermi arcs while keeping the rest unchanged. Our paper hence helps clarify the intricate interplay between topology and NHSE in non-Hermitian systems, and provides a versatile approach for designing non-Hermitian topological systems where topological properties and NHSE do not interfere each other.

I. INTRODUCTION

The bulk-boundary correspondence (BBC) is among the most important principles in the investigation of topological phases of matter [1–6]. Namely, a topological invariant defined under the periodic boundary conditions (PBCs) predicts the number of topological boundary modes under the open boundary conditions (OBCs). Accordingly, topological phase transitions involve band gap closing for both PBC and OBC bulk spectra, which is the only possibility to change the topological invariant and the number of topological modes.

In recent years, investigations into non-Hermitian topological phases reveal an enigmatic violation of conventional BBC [7–12], as the eigenvalues and eigenvectors of most non-Hermitian systems are extremely sensitive to boundary conditions [13–15]. In particular, the topological structure of PBC energy bands can be changed by passing through exceptional points (EPs) when gradually eliminating the amplitude of hopping between the ends of a chain to reach OBCs, which leads to the connection of different bands in the complex energy plane [13]. In these systems, OBC eigenstates tend to be exponentially localized near system's boundaries, which is called the non-Hermitian skin effect (NHSE) [8,16], and the number of topological edge modes may no longer be related to the topological invariants formulated in terms of the Bloch Hamiltonian, as the gap-closing condition can be different for PBCs and OBCs. A modified BBC has been established for these systems through the non-Bloch band theory [7,16–18]. In such a framework, topological invariants are defined with complex deformations of lattice momentum, which generally have rather intricate explicit forms and extremely sensitive numerical solutions for systems beyond minimal models [19,20],

making it difficult to accurately identify their topological properties.

In this paper, we unveil a class of topological compatible NHSE (TC-NHSE), where massive edge localization of eigenstates emerges without breaking the conventional BBC, as non-Hermiticity is introduced properly to avoid inducing any EP to the system. We first discuss the general scheme for inducing two types of TC-NHSE in two-band non-Hermitian Hamiltonians, where conventional BBC is preserved either universally or only within certain parameter regimes, respectively. An explicit one-dimensional (1D) example of a non-Hermitian Su-Schrieffer-Heeger (SSH) model [21] is then demonstrated accordingly. We next extend the 1D SSH model into a 2D semimetallic system with an extra spin degree of freedom and spin-orbit coupling terms, where three sets of Weyl points protected by different (hidden) $\mathcal{PT}$ symmetries emerge between different energy bands. More interestingly, TC-NHSE can be introduced in a way that is selectively compatible to different sets of Weyl points, transforming some of them into EPs by breaking the corresponding symmetry while the others remain unchanged. The topological compaticity of the induced NHSE is further verified by calculating the non-Hermitian Zak phase defined with Bloch eigenstates, which precisely predict topological properties under OBCs, for both the 1D and 2D models.

II. GENERAL TWO-BAND HAMILTONIANS

We begin with a general non-Hermitian two-band Hamiltonian,

$$h(k) = \sum_{\alpha=0,x,y,z} h_\alpha(k)\sigma_\alpha,$$

$$h_\alpha = d_\alpha(k) + ig_\alpha(k), \tag{1}$$

[*]Corresponding author: lilh56@mail.sysu.edu.cn

with $d(k)$ and $g(k)$ taking real values, describing the Hermitian and anti-Hermitian parts of the system, $\sigma_{x,y,z}$ the Pauli matrices, and σ_0 the 2×2 identity matrix. We will omit the k dependency in the notations of d_α, g_α, and h_α for simplicity. A topological phase transition requires a band touching point of $h(k)$, which occurs when

$$P(k) = \sum_{\alpha=x,y,z} h_\alpha^2 = 0,$$

namely

$$\sum_{\alpha=x,y,z} \left(d_\alpha^2 - g_\alpha^2\right) = 0, \quad \sum_{\alpha=x,y,z} d_\alpha g_\alpha = 0, . \quad (2)$$

This condition generally applies to an exceptional degeneracy point (EP) of $h(k)$. A normal degenerate point (DP) appears when the system further satisfies $h_\alpha = 0$ for $\alpha = x, y, z$.

The breakdown of conventional BBC requires different bands connect head to tail in the complex energy plane [7,13,22], corresponding to a nontrivial winding of eigenvectors around an EP [23–25]. As Hermitian systems forbid any EP to exist, this means that if we start from a Hermitian $h(k)$ and turn on non-Hermiticity gradually, it must go through a EP transition to break conventional BBC. In turn, in order for NHSE to emerge without breaking the conventional BBC, we need to properly introduce non-Hermiticity to the system, and avoid inducing any EP. For our minimal two-band Hamiltonian, this can be done by introducing

(i) a nonzero g_0 that shifts both bands by the same amount for each momentum k, or

(ii) nonzero g_x, g_y, or g_z, which vanishes together with the Hermitian parts of the Hamiltonian, i.e., when $d_x = d_y = d_z = 0$.

In both cases, NHSE can emerge provided that the non-Hermitian terms also induce nontrivial spectral winding to the PBC spectrum. Note that the first scheme shall avoid EP under any circumstance, as g_0 only shifts the eigenvalues of $h(k)$, but does not change its degenerate condition. On the other hand, the second scheme does not always guarantee the absence of EP, and the NHSE may be topologically compatible only in a certain parameter regime, as elaborated with the example model discussed below.

III. TC-NHSE IN A 1D TWO-BAND MODEL

To give an explicit example, we consider a non-Hermitian extension of the Su-Schrieffer-Heeger (SSH) model [21] as sketched in Fig. 1, described by the Hamiltonian $H_{\mathrm{1D}} = H_{\mathrm{SSH}} + H_{\mathrm{nonH}}$ where

$$H_{\mathrm{SSH}} = \sum_n^N (t_1 \hat{a}_n^\dagger \hat{b}_n + t_2 \hat{b}_n^\dagger \hat{a}_{n+1}) + \text{H.c.}, \quad (3)$$

$$H_{\mathrm{nonH}} = \sum_n^N \delta_1 (\hat{a}_n^\dagger \hat{a}_{n+1} + \hat{b}_n^\dagger \hat{b}_{n+1}) - \text{H.c.}$$

$$+ \sum_n^N \delta_2 (\hat{a}_n^\dagger \hat{b}_{n+1} - \hat{a}_n^\dagger \hat{b}_{n-1}) - \text{H.c.}, \quad (4)$$

with a and b the two sublattices of the system, and N the total number of unit cells. Its Bloch Hamiltonian in momentum
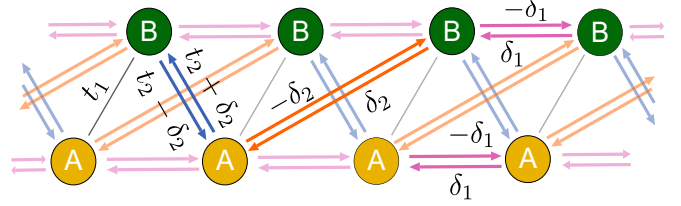

FIG. 1. A sketch of the 1D lattice of the non-Hermitian SSH model described by Eqs. (3) and (4). The arrows of different colors indicate different hopping parameters. Opaque arrows are marked by the parameters they represent, and unmarked ones are made translucent for a clearer demonstration.

space reads

$$h_{\mathrm{1D}}(k) = (t_1 + t_2 \cos k)\sigma_x + t_2 \sin k \sigma_y$$
$$+ i(2\delta_1 \sin k \sigma_0 + 2\delta_2 \sin k \sigma_x), \quad (5)$$

and the gap-closing conditions are given by

$$(t_1 + t_2 \cos k)^2 + (t_2^2 - 4\delta^2) \sin^2 k = 0,$$
$$4\delta \sin k(t_1 + t_2 \cos k) = 0. \quad (6)$$

For $|2\delta_2| < |t_2|$, the above conditions are satisfied only at the DPs of the Hamiltonian, namely when $d_x = d_y = g_x = 0$ at $(t_1, k) = (t_2, \pi)$ or $(-t_2, 0)$. In other words, conventional BBC is expected to be valid in this parameter regime, as shown by the PBC and OBC spectra in Figs. 2(a) and 2(b). The 1D topological properties can be characterized by the non-Hermitian
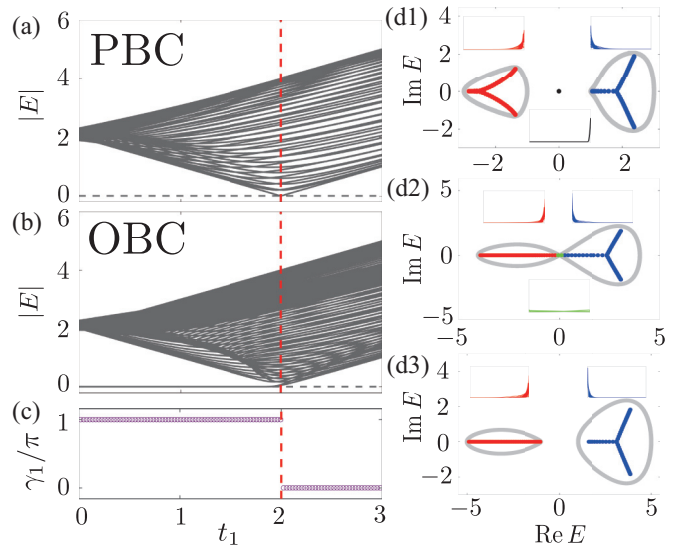

FIG. 2. TC-NHSE in the non-Hermitian SSH model. [(a),(b)] The absolute values of eigenenergies $|E|$ under PBCs and OBCs respectively, with the same gap-closing point at $t_1 = 2$ (red-dashed lines). In either case, $|E|$ of the two energy bands roughly overlap each other. (c) The Zak phase γ_1 as a function of t_1. [(d1)–(d3)] The complex spectrum under the PBCs (gray) and OBCs (red, blue, black, and green) for $t_1 = 1, 2,$ and 3 respectively, with insets demonstrating distribution profiles of OBC eigenstates with the same colors. Other parameters are $t_2 = 2$, $\delta_1 = 0.75$, $\delta_2 = 0.5$, $N = 60$.
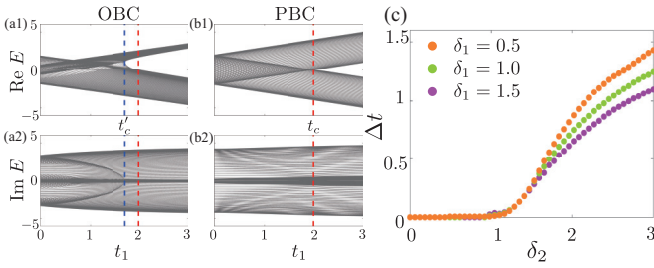
FIG. 3. [(a),(b)] PBC and OBC eigenenergies vs t_1, with $\delta_2 = 1.5 > t_2/2$ and $\delta_1 = 1$. The gap-closing points $t_1 = t_c$ and $t_1 = t_c'$ under the PBCs and OBCs are denoted by red and blue-dashed lines, respectively, which do not coincide. (c) The deviation between the PBC and OBC gap-closing points $\Delta t = t_c - t_c'$, as a function of δ_2 for three different values of δ_1. Other parameters : $t_2 = 2$, $N = 120$.

Zak phase, defined as [10]

$$\gamma_n = -\mathrm{Im} \oint_{\mathrm{BZ}} \langle \psi_{L,n}(k)|\partial_k|\psi_{R,n}(k)\rangle dk,$$

with $\psi_{R,n}$ ($\psi_{L,n}$) the right (left) biorthogonal [26] Bloch eigenstate of the nth energy band. In particular, in our considered two-band cases, the non-Hermitian Zak phase can be analytically expressed as a winding number of the real part of the Hamiltonian vector, as shown in Appendix A. As evident in Fig. 2(c), γ_n takes quantized values of π and 0 in the regimes with and without zero-mode edge states under OBC, respectively, reflecting the existence of conventional BBC. On the other hand, bulk states accumulate to the two ends of the 1D lattice under OBC, indicating the emergence of TC-NHSE, as shown in Fig. 2(d). In addition, for the topological phase transition in Fig. 2(d2), eigenstates are seen to be delocalized

at the gap-closing point ($k = \pi$), where the non-Hermitian terms in Eq. (5) vanish.

Further increasing the absolute value of δ_2, an EP transition occurs at $|\delta_2| = |t_2/2|$ with two EPs at $\cos k = -t_1/t_2$. Consequently, the conventional BBC is broken for $|\delta_2| > |t_2/2|$, as shown in Figs. 3(a) and 3(b). On the other hand, δ_1 does not enter the gap-closing conditions of Eqs. (6), thus it never breaks conventional BBC. In Fig. 3(c), we display numerical results of the deviation between PBC and OBC gap-closing point as a function of δ_2, which acquires a nonvanishing value when $\delta_2 > t_2/2$, regardless of the values of δ_1. Nonetheless, we point out that each of δ_1 and δ_2 alone can induce NHSE in this model, as further demonstrated in Appendix B.

IV. TC-NHSE IN SEMIMETALS

Extending the 1D SSH model into 2D by introducing the same lattice structure along a second direction, we obtain a 2D Hamiltonian

$$\begin{aligned} h_{2\mathrm{D}}(k_x, k_y) &= (t_1 + t_2 \cos k_x + t_2 \cos k_y)\sigma_x \\ &\quad + (t_2 \sin k_x + t_2 \sin k_y)\sigma_y. \end{aligned} \tag{7}$$

This Hamiltonian generally describes a semimetal with two gapless points located along $k_x = -k_y$. Following previous discussion, non-Hermiticity can be introduced in the same manners as for the 1D case to induce compatible NHSE, which does not affect these gapless points. To go beyond these two basic types of compatible NHSE, we take into account the spin degree of freedom, and consider two types of spin-orbit terms $h_{\mathrm{SO}} = h_{\mathrm{SO},1} + h_{\mathrm{SO},2}$,

$$\begin{aligned} h_{\mathrm{SO},1} &= t_{\mathrm{SO}}(\sin k_x \tau_y - \sin k_y \tau_x), \\ h_{\mathrm{SO},2} &= v_{\mathrm{SO}} \sin(k_x + k_y + \phi)\tau_z\sigma_z, \end{aligned} \tag{8}$$

with t_{SO} and v_{SO} describing their strengths, and ϕ a phase factor to tune the position of Weyl points in momentum space. Its eigenenergies read (subscribes ordered by their real energies)

$$E_{1,2,3,4}(k_x, k_y) = \pm\sqrt{\begin{aligned}&[\sqrt{(t_1 + t_2 \cos k_x + t_2 \cos k_y)^2 + (t_2 \sin k_x + t_2 \sin k_y)^2} \pm \sqrt{(t_{\mathrm{SO}} \sin k_x)^2 + (t_{\mathrm{SO}} \sin k_y)^2}]^2 \\ &+ [v_{\mathrm{SO}} \sin(k_x + k_y + \phi)]^2\end{aligned}}. \tag{9}$$

The original gap-closing points become fourfold degenerate Dirac points when the spin degree of freedom is introduced, which evolve into twofold degenerate Weyl points at zero-energy under nonzero v_{SO} and t_{SO}, whose location in the Brillouin zone is determined by

$$\text{Set I}: \quad v_{\mathrm{SO}} \sin(k_x + k_y + \phi) = 0, \tag{10}$$

$$\begin{aligned} &(t_1 + t_2 \cos k_x + t_2 \cos k_y)^2 + (t_2 \sin k_x + t_2 \sin k_y)^2 \\ &= (t_{\mathrm{SO}} \sin k_x)^2 + (t_{\mathrm{SO}} \sin k_y)^2. \end{aligned} \tag{11}$$

Numerically, we find that these Weyl points can be locally gapped out only by terms anticommuting with $h_{\mathrm{SO},2}$, namely $\sigma_\alpha \tau_{\bar{\alpha}}$ with $\alpha, \bar{\alpha} \in \{x, y, z\}$, $\alpha \neq \bar{\alpha}$, and either α or $\bar{\alpha}$ being z. Thus the existence of the zero-energy Weyl points can be

attributed to the protection of an parity-time (PT) symmetry,

$$\sigma_x \tau_x h^*(k)\sigma_x \tau_x = h(k), \tag{12}$$

which excludes the above mentioned matrices from the Hamiltonian.

Other than these zero-energy gap-closing points, extra Weyl points also emerge between the first (last) two bands when

$$\begin{aligned} \text{Set II}: \quad &t_1 + t_2 \cos k_x + t_2 \cos k_y \\ &= t_2 \sin k_x + t_2 \sin k_y = 0, \end{aligned}$$

or

$$\text{Set III}: \quad t_{\mathrm{SO}} \sin k_x = t_{\mathrm{SO}} \sin k_y = 0.$$

Note that these two sets of Weyl points are determined solely by $h_{2\mathrm{D}}$ and $h_{\mathrm{SO},1}$, respectively. In order words, Weyl points of
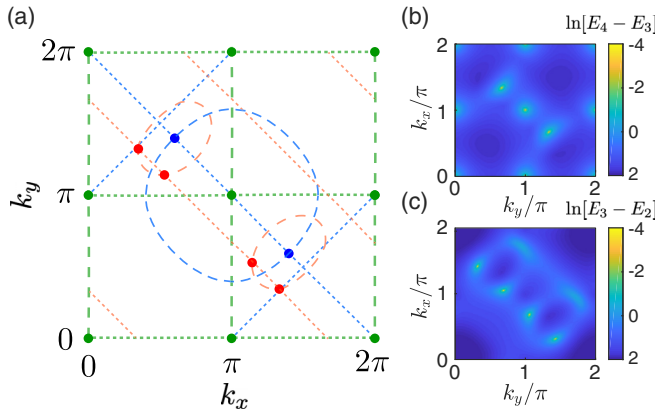
FIG. 4. (a) Schematic of the position (points) and degenerate conditions (dash lines) of Sets I (red), II (blue), and III (green) Weyl points in momentum space. (b) Energy difference between E_3 and E_4, zeros indicate the Weyl points of Sets II and III [blue and green points in (a)]. (c) Energy difference between E_2 and E_3, zeros indicate the Weyl points of Set I [red points in (a)]. Note that due to the resolution of the figure, there seems to be six bright spots in panel (c), where the two curvyish ones no matching the red points in (a) represent regions with a small but nonzero band gap between E_2 and E_3. Parameters for (b) and (c) are $t_1 = t_2 = t_{SO} = 2$, $v_{SO} = 1.2$, and $\phi = \pi/4$.

Sets II and III are protected by hidden PT symmetries of the corresponding sub-Hamiltonians,

$$\sigma_x h_{2D}^*(k_x, k_y)\sigma_x = h_{2D}(k_x, k_y), \quad (13)$$

$$\tau_x h_{SO,1}^*(k_x, k_y)\tau_x = h_{SO,1}(k_x, k_y), \quad (14)$$

respectively. The locations in the Brillouin zone of these three sets of Weyl points are sketched in Fig. 4(a). In Figs. 4(b) and 4(c), we demonstrate the energy difference between the highest and middle two bands, respectively, where zeros of the former (later) represents Weyl points of Sets II or III (Set I). Given the coexistence of Weyl points between different bands, we argue that NHSE can not only be introduced in a way that is compatible to all sets of Weyl points, e.g., through introducing a non-Hermitian τ_0 term, but also in a way that is selectively compatible to different sets of Weyl points, transforming some of them into EPs while the others remain unchanged. As a first demonstration, we consider the following non-Hermitian term as an example,

$$h_{nonH1} = i\delta_1 \tau_z \sigma_z, \quad (15)$$

which breaks the PT symmetry and transforms the first set of Weyl points (at Re[E] = 0) into bulk Fermi arcs [27–29] with degenerate real energies, as shown in Figs. 5(a) and 5(b). In contrast to boundary Fermi arcs in Hermitian systems, bulk Fermi arcs are terminated at EPs with zero imaginary energy, whose locations are determined by

$$k_x + k_y + \phi = 0,$$

$$|E_{2,3}(k_x, -k_x - \phi)| = |\delta_1|,$$

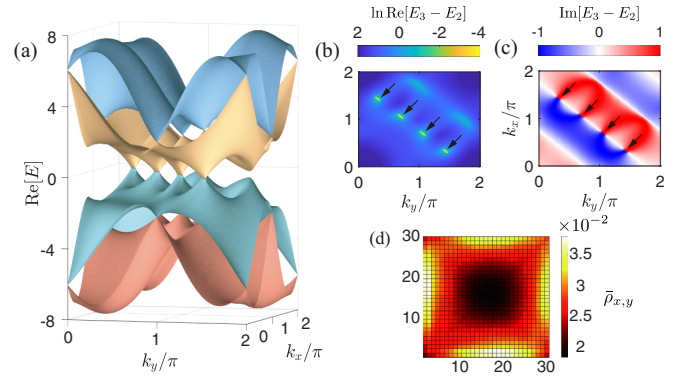and the two bands sorted by their real energies have discontinuous imaginary energies across the arcs, as shown in Fig. 5(c).

FIG. 5. The properties of the system when introducing the non-Hermitian term h_{nonH1} with $\delta_1 = 0.5$. (a) The real part of the energy bands structure, valence and conduction bands meet at bulk Fermi arcs. The logarithm of real energy difference (b) and the imaginary energy difference (c) between the middle two bands E_2 and E_3. Black arrows indicate the regions of bulk Fermi arcs, where the imaginary energies switch between the two bands, as shown by the jump of Im[$E_3 - E_2$] between large negative and positive values across the bulk Fermi arcs. (d) The average distribution $\bar{\rho}_{x,y}$ of all eigenmodes under OBCs. Other parameters: $t_1 = t_2 = t_{SO} = 2$, $v_{SO} = 1.2$, and $\phi = \pi/4$.

On the other hand, h_{nonH1} does not alter the hidden symmetries of the sub-Hamiltonians, therefore the other two sets of Weyl points remains unchanged, as can be seen in Fig. 5(a) between the top two or the bottom two bands. In Fig. 5(d), we display the average distribution of all eigenmodes under OBCs,

$$\bar{\rho}_{x,y} = (1/N) \sum_i^N \sqrt{\sum_\alpha |\psi_{x,y,\alpha}^i|^2},$$

with N the size of the Hilbert space, and $\psi_{x,y,\alpha}^i$ the wave amplitude of the ith eigenmode at unit cell (x, y), $\alpha = (\tau, \sigma)$ denoting the spin and sublattice degrees of freedom respectively. A clear edge localization can be seen in the figure, indicating the emergence of NHSE compatible with the second and third sets of topological Weyl points. Similarly, by breaking different hidden PT symmetries of Eqs. (13) and (14), the resultant non-Hermitian system may host NHSE [see Figs. 6(a3) and 6(b3)] compatible with Set I and only one of the rest two sets of Weyl points. Specifically, we consider the following two non-Hermitian terms,

$$h_{nonH2} = i2\delta_2 \sin(k_x + k_y + \phi)\sigma_x, \quad (16)$$

$$h_{nonH3} = i2\delta_3 \sin(k_x + k_y + \phi)\tau_x. \quad (17)$$

Note the these extra terms also inevitably break the PT symmetry of Eq. (12) for the overall system. To avoid destroying the zero-energy Weyl points of Set I, the explicit forms of h_{nonH2} and h_{nonH3} are chosen to vanish (thus recovering the symmetry) at the momenta of these points. In Figs. 6(a1) and 6(a2), the degenerate real energies and discontinuous imaginary energies show that Weyl points of Set II [blue dots in Fig. 4(a)] are transformed into EPs connected by bulk Fermi arcs due to h_{nonH2}, which breaks the corresponding hidden PT symmetry of Eq. (13), similar to the influence of h_{nonH1} on the

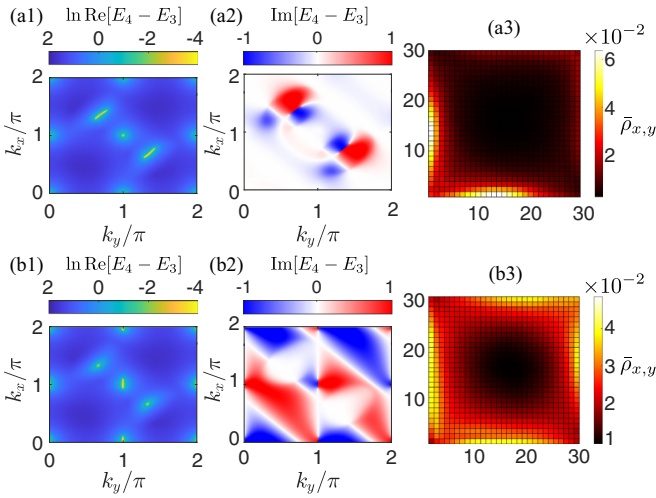FIG. 6. The properties of the system when introducing the non-Hermitian term h_{nonH2} (a) or h_{nonH3} (b) with $\delta_2 = 0.35$ or $\delta_3 = 0.35$. The logarithm of real energy difference [(a1),(b1)] and the imaginary energy difference [(a2),(b2)] between the last two bands E_3 and E_4. [(a3),(b3)] The average distribution $\bar{\rho}_{x,y}$ of all eigenmodes under OBCs. Other parameters: $t_1 = t_2 = t_{\mathrm{SO}} = 2$, $v_{\mathrm{SO}} = 1.2$, $\phi = \pi/4$.

first set of Weyl points. Besides, NHSE is seen to emerge as the average distribution of all eigenmodes $\bar{\rho}_{x,y}$ localizes at the left and bottom boundaries [Fig. 6(a3)], and is topologically

compatible with the other two sets of Weyl points (Sets I and III) that remain unchanged as in the Hermitian case. Similarly, introducing non-Hermitian term h_{nonH3} will break the hidden PT symmetry of Eq. (14), and only transform Weyl points of Set III into bulk Fermi arcs, as shown in Figs. 6(b1) and 6(b2). Thus the resultant NHSE, with $\bar{\rho}_{x,y}$ localizing at all of the four boundaries [Fig. 6(b3)], is compatible with Weyl points of Sets I and II. We also note that extra EPs and bulk Fermi arcs (irrelevant to the Weyl points) may appear between different bands when further increasing each of the non-Hermitian parameters $\delta_{1,2,3}$ (not shown).

To further demonstrate the topological compatibility of NHSE induced by different non-Hermitian terms, we compare the absolute values of eigenspectra under full PBC and x-PBC/y-OBC in Fig. 7. It is seen that in the presence of each non-Hermitian term, only one set of Weyl points are transformed into EPs under full PBC, where the gap-closing points diverge under different boundary conditions. For example, in Fig. 7(a) with nonzero δ_1, a pair of EPs (transformed from a Weyl point of Set I) at $|E_{\mathrm{PBC}}| = 0$ under full PBC in Fig. 7(a2) are marked by red dash lines, which do not coincide with the gap-closing points of $|E_{\mathrm{OBC}}| = 0$ under x-PBC/y-OBC in Fig. 7(a3). In comparison, the Weyl points (Sets II and III) at nonzero $|E|$, which are partially marked by blue and green circles, remain unchanged under different boundary conditions.

Taking k_x as a parameter, topological properties related to these gap-closing points can be characterized by the Zak phase
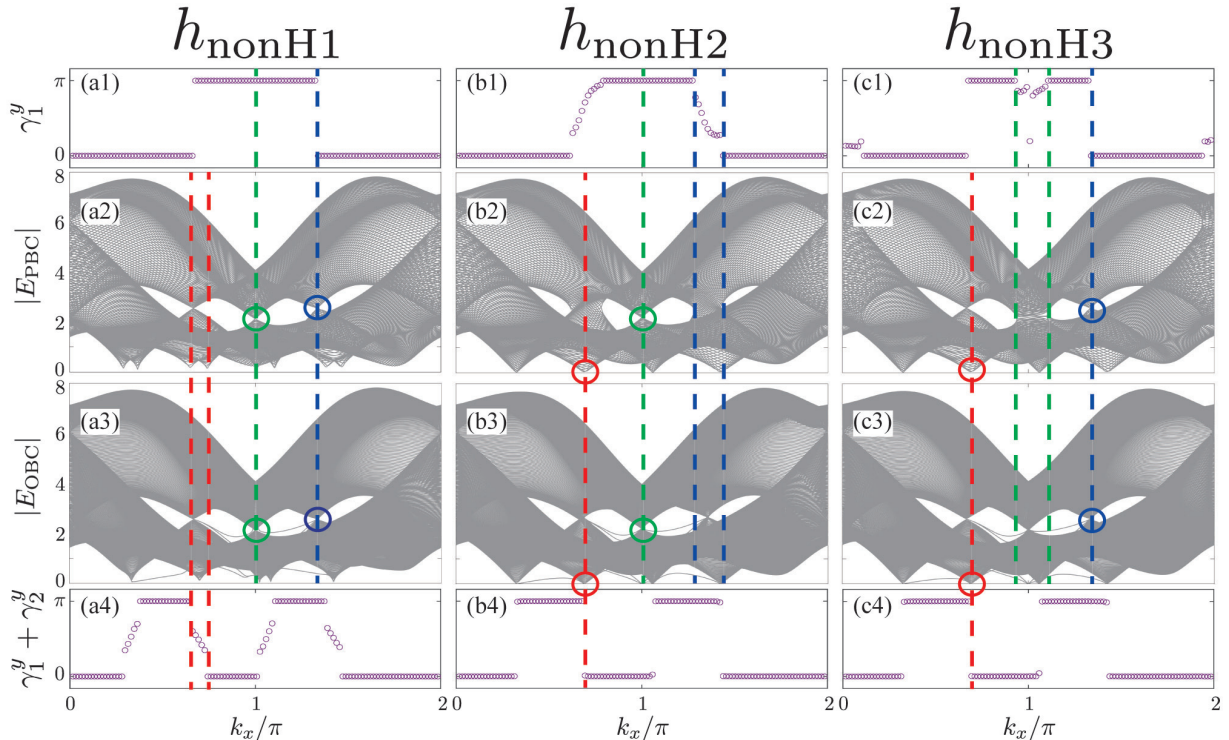

FIG. 7. The absolute value of full PBC (a2) (b2) (c2) and x-PBC/y-OBC (a3) (b3) (c3) spectrum as a function of k_x with introducing the non-Hermitian terms h_{nonH1} (a), h_{nonH2} (b), and h_{nonH3} (c) into the Hermitian Hamiltonian $h_{\mathrm{2D}} + h_{\mathrm{SO}}$, corresponding to the change of Zak phase γ_1^y (a1) (b1) (c1) and $\gamma_1^y + \gamma_2^y$ (a4) (b4) (c4). The red (Set I), blue (Set II) and green (Set III) dash lines indicate the gap-closing points under the PBC in y direction around one of each set of Weyl points, which are marked by circles if they remain unchanged under OBC. It shows that different sets of Weyl points are transformed into EPs by different non-Hermitian terms and the Zak phase is not quantized when EPs appear. The length in y direction is $N = 150$ and the non-Hermitian parameters are $\delta_1 = 0.5$ (a), $\delta_2 = 0.35$ (b), and $\delta_3 = 0.35$ (c) respectively. Other parameters: $t_1 = t_2 = t_{\mathrm{SO}} = 2$, $v_{\mathrm{SO}} = 1.2$, $\phi = \pi/4$.

as in the 1D case, defined as

$$\gamma_n^y(k_x) = -\text{Im} \oint_0^{2\pi} dk_y \langle \psi_{L,n}(k_x, k_y) | \partial_{k_y} | \psi_{R,n}(k_x, k_y) \rangle.$$

As seen in Fig. 7(a1), γ_1^y (which describes the topological properties of the lowest energy band) is always quantized at π or 0, and jumps between them only at the gap-closing points (Weyl points) at nonzero $|E_{\text{PBC/OBC}}|$ [partially marked by blue and green circles in Figs. 7(a2) and 7(a3)]. Note that it remains unchanged across the gap-closing point at $k_x = \pi$, which is actually the projection of a pair of Weyl points with opposite topological charges [at $k_y = 0$ and π, see green dots in Fig. 4(a)]. On the other hand, as shown in Fig. 7(a4), the summed Zak phase between the lower two bands ($\gamma_1^y + \gamma_2^y$) becomes nonquantized in the parameter regime between each pair of EPs with $|E_{\text{PBC}}| = 0$, and its transition points do not match the gap-closing points under OBC with $|E_{\text{OBC}}| = 0$ in Fig. 7(a3).

Similar phenomena are also observed with nonzero δ_2 and δ_3, where the non-Hermiticity is compatible with different sets of Weyl points, respectively. As shown in Fig. 7(b), nonzero δ_2 leads to a nonquantized Zak phase γ_1^y in the parameter regimes between the EPs marked by blue-dashed lines (Set II), while $\gamma_1^y + \gamma_2^y$ is always quantized and only jumps discontinuously at the Weyl points with $|E_{\text{PBC/OBC}}| = 0$ (Set I, red circles). On the other hand, nonzero δ_3 leads to a nonquantized γ_1^y when k_x falls between the EPs marked by green dash lines (Set III), while $\gamma_1^y + \gamma_2^y$ also remains quantized and correctly reflects both the PBC and OBC topological properties, as shown in Fig. 7(c). These observations further validate the topological compatibility of NHSE induced by different non-Hermiticity in our model with different sets of Weyl points.

V. SUMMARY

To summarize, we have revealed a class of TC-NHSE, which induces nontrivial spectral winding and skin accumulation of eigenstates to the system without breaking conventional BBC. By analyzing the degenerate condition of general non-Hermitian two-band Hamiltonians, we have provided a general scheme for introducing NHSE without inducing any EP, and demonstrate the corresponding TC-NHSE in a 1D non-Hermitian SSH model. Specifically, the induced NHSE is compatible with the system's topology either in a universal manner, or only in a certain parameter regime, depending on how the non-Hermiticity enters the Hamiltonian explicitly. Next, we extended the 1D SSH model into a 2D $\mathcal{PT}$-symmetric semimetal with three sets of Weyl points between different energy bands, protected by different symmetries or hidden symmetries of the system respectively. We find that by introducing non-Hermitian terms that break different symmetries of the system, the corresponding TC-NHSE can be selectively compatible to one set of Weyl points (i.e., remain unchanged in the momentum space) and transform the rest into pairs of EPs connected by bulk Fermi arcs. By taking k_x as a parameter, the unaffected Weyl points can be characterized by the quantized non-Hermitian Zak phase, which becomes nonquantized in the parameter regime between each pair of EPs transformed from a Weyl point, reflecting the selective compatility of the TC-NHSE in the system.

The topological properties of our studied systems are characterized by the non-Hermitian Zak phase, which essentially describes 1D topology corresponding to edge states gapped from the bulk (as in 1D topological insulators), or bulk degeneracy with codimension of two (as in 2D semimetals). Nevertheless, our scheme for inducing TC-NHSE relies only on the vanishing of non-Hermiticity at bulk degeneracy, and thus it can also be straightforwardly extended to other higher-dimensional topological phases, such as 2D topological insulators characterized by the Chern number. A potential area of interest is the generalization of TC-NHSE in more sophisticated topological phases, such as higher-order topological phases where topological edge states may not directly correspond to bulk topology [30–35], or hybrid skin-topological phases where NHSE interplay with topological localization in a distinctive manner [36–38].

Finally, we note that in this study, we have considered a few toy models for a clear demonstration of the TC-NHSE. Nevertheless, during the past few years, different types of NHSE have been realized in a variety of experimental platforms, such as electrical [39–43], photonic [44–47], and acoustic [48–51] systems, each has flexible parameters that can be individually tuned, thus making them promising for constructing our models. Another charming platform with the potential for realizing the TC-NHSE is quantum gases in optical lattices, which further allow for experimentally investigating the rich interplay between quantum many-body effect and NHSE [52–56]. In particular, the SSH-type staggered hopping amplitudes in 1D and the spin-orbit terms of our 2D models can be realized with double-well optical potentials [57–59] and Raman lasers that couple different orbitals [60–63], respectively. Designing the optical potential for our 2D extension of the SSH model [Eq. (7)] may be challenging, as staggered hopping amplitudes along two directions will result in four sublattices instead of two. However, similar 1D topological properties also exist in the Creutz ladder model [22,64], whose realization involves no sublattice structure, but different orbitals of the same lattice sites with periodically driven lattice potential [65,66], making its higher-dimensional generalization more straightforward. In addition, non-Hermiticity can be implemented in cold atoms with laser-assisted atom loss [67,68], which has already been applied for realizing NHSE in 1D momentum space of a untracold atomic gases [69]. These developments indicate the possibility for realizing TC-NHSE in cold atoms, but an explicit scheme still remains to be considered in depth.

APPENDIX A: THE NON-HERMITIAN ZAK PHASE EXPRESSED AS A WINDING NUMBER FOR CHIRAL NON-HERMITIAN SYSTEM

Here we consider a general non-Hermitian two-band Hamiltonian in momentum space, which can be written in the

form of Eq. (1),

$$h(k) = \sum_{\alpha=0,x,y,z} h_\alpha(k)\sigma_\alpha,$$

$$h_\alpha = d_\alpha(k) + ig_\alpha(k). \tag{A1}$$

Its left and right eigenstates are given by

$$|\psi_+^R\rangle = \begin{pmatrix} e^{-i\phi}\cos\frac{\theta}{2} \\ \sin\frac{\theta}{2} \end{pmatrix}, \quad |\psi_-^R\rangle = \begin{pmatrix} e^{-i\phi}\sin\frac{\theta}{2} \\ -\cos\frac{\theta}{2} \end{pmatrix}, \tag{A2}$$

and

$$\langle\psi_+^L| = \begin{pmatrix} e^{i\phi}\cos\frac{\theta}{2} \\ \sin\frac{\theta}{2} \end{pmatrix}, \quad \langle\psi_-^L| = \begin{pmatrix} e^{i\phi}\sin\frac{\theta}{2} \\ -\cos\frac{\theta}{2} \end{pmatrix}, \tag{A3}$$

with $\cos\theta = h_z/\sqrt{h_x^2 + h_y^2 + h_z^2}$ and $\cos\phi = h_x/\sqrt{h_x^2 + h_y^2}$, and $\pm$ denoting the two bands. We note that h_0 does not enters the expressions of eigenstates, and we will omit this term in our following discussion. Here we consider the non-Hermitian Zak phase of the lower band, which can be obtained as [70]

$$\gamma^{(-)} = -\text{Im}\oint_{\text{BZ}}\langle\psi_-^L|\partial_k|\psi_-^R\rangle dk$$

$$= \text{Re}\oint_{\text{BZ}}\frac{\partial\phi}{\partial k}\sin^2\frac{\theta}{2}dk. \tag{A4}$$

If the Hamiltonian has chiral symmetry $\sigma_z h(k)\sigma_z = -h(k)$, we have $\cos\theta = 0$, and $\gamma^{(-)}$ is given $\text{Re}\oint_{\text{BZ}}\frac{d\phi}{2}$, namely half the total winding angle of (h_x, h_y) when k varies from 0 to 2π, or in other words, the winding number of (h_x, h_y) multiplied by π. For non-Hermitian systems, ϕ may take complex values, making the winding number of (h_x, h_y) ill defined. Thus we further consider the winding number of (d_x, d_y), i.e., the Hermitian parts of a chiral-symmetric Hamiltonian, and their winding number ν in the parameter space takes the form as

$$\nu = \frac{1}{2\pi}\oint_{\mathcal{C}}d\phi' \tag{A5}$$

$$= \frac{1}{2\pi}\int_0^{2\pi}dk\frac{d_x\partial_k d_y - d_y\partial_k d_x}{d_x^2 + d_y^2}, \tag{A6}$$

where $\mathcal{C}$ is the trajectory of (d_x, d_y) in a period. Further considering the non-Hermitian terms g_x and g_y vanish together with the Hermitian parts of the Hamiltonian (so to generate TC-NHSE),

$$g_x = a d_y, \quad g_y = b d_x, \tag{A7}$$

where a and b are chosen to be real and positive without loss of generality, the Zak phase can be expressed as

$$\gamma^{(-)} = \frac{\text{Re}}{2}\oint_{\text{BZ}}\frac{(1+ab)(d_x\partial_k d_y - d_y\partial_k d_x)}{(1-b^2)d_x^2 + (1-a^2)d_y^2 + 2i(a+b)d_x d_y}. \tag{A8}$$

Substituting $d\phi' = dk(d_x\partial_k d_y - d_y\partial_k d_x)/(d_x^2 + d_y^2)$ into Eq. (A8), we obtain

$$\gamma^{(-)} = \frac{\text{Re}}{2}\int_{\phi'(k=0)}^{\phi'(k=2\pi)}\frac{(1+ab)d\phi'}{(1-b^2)\cos^2\phi' + (1-a^2)\sin^2\phi' + 2i(a+b)\sin\phi'\cos\phi'}, \tag{A9}$$

which is nonzero only when the winding of ϕ' is nontrivial (i.e., $\nu \neq 0$), as $\phi'(0) = \phi'(2\pi)$. To further simplify the above integral, we substitute $z = \tan\phi'$ into Eq. (A9) and obtain

$$\gamma^{(-)} = \frac{1}{2}\text{Re}\int dz\frac{1+ab}{(1-b^2) + (1-a^2)z^2 + 2i(a+b)z}$$

$$= \text{Re}\frac{1+ab}{2(1-a^2)}\int dz\frac{1}{(z-z_1)(z-z_2)}.$$

Here z_1 and z_2 are the two roots of the denominator polynomial, which take pure imaginary values, given by

$$z_{1,2} = i\frac{-(a+b) \pm (ab+1)}{1-a^2}. \tag{A10}$$

In nontrivial cases with $\nu \neq 0$, ϕ' varies in the interval $[\phi_0, \phi_0 + 2\nu\pi]$, and z varies ν times in infinite intervals $[\tan\phi_0, +\infty)$, and $(-\infty, \tan\phi_0]$, so

$$\gamma^{(-)} = \text{Re}\frac{1+ab}{2(1-a^2)}\int_{\phi=\phi_0}^{\phi=\phi_0+2\nu\pi}dz\frac{1}{(z-z_1)(z-z_2)}$$

$$= \text{Re}\frac{1+ab}{2(1-a^2)}\oint_{\mathcal{L}+\mathcal{C}'}dz\frac{\nu}{(z-z_1)(z-z_2)}, \tag{A11}$$

where $\mathcal{L}$ is the real axis and $\mathcal{C}'$ is a semicircle of infinite radius on the lower complex plane. The integral of Eq. (A11) can be calculated by residue theorem

$$\gamma^{(-)} = \text{Re}\frac{1+ab}{1-a^2}\cdot 2\pi i\sum_j\text{Res}\left[\frac{\nu}{(z-z_1)(z-z_2)}\right]$$

$$= \begin{cases} -\nu\pi, & a, b > 1 \\ \nu\pi, & a, b < 1 \\ 0, & a > 1, b < 1 \quad \text{or} \quad a < 1, b > 1, \end{cases} \tag{A12}$$

where z_j is the residue of the function $\frac{1}{(z-z_1)(z-z_2)}$ on the lower complex plane. For the non-Hermitian SSH model we discussed in Sec. III, the parameters are given by $a = 0$ and $b = 2\delta_2/t_2$. We can see that the Zak phase can be mapped to the winding number ν when $\delta_2 < t_2/2$, i.e., the parameter regime with TC-NHSE where the conventional BBC is valid. However, when $\delta_2 > t_2/2$, the Zak phase $\gamma^{(-)}$ is always 0, and can no longer predict the existence of zero-mode edge states.

APPENDIX B: TC-NHSE IN THE 1D NON-HERMITIAN SSH MODEL

In this Appendix, we provide further analysis of the NHSE induced by δ_1 and δ_2 in the model described by Eq. (5). As shown in Figs. 8(a1) and 8(b1), each of these two non-Hermitian parameters along can induce NHSE in the system, yet the resultant skin modes show different localizing
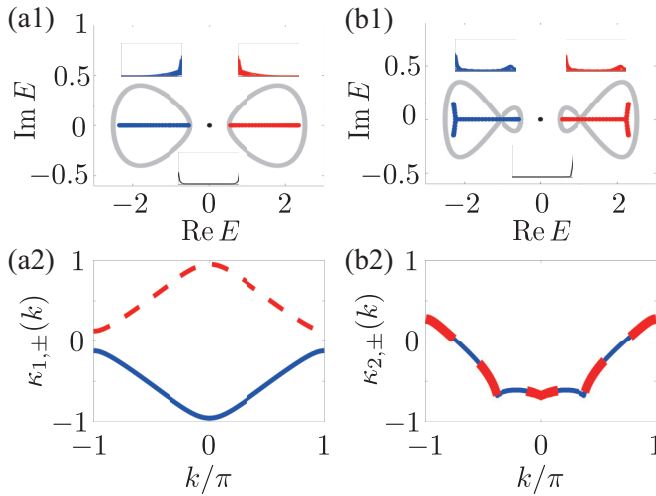
FIG. 8. [(a1),(b1)] Complex spectra under the PBCs (gray) and OBCs (red, blue, and black) for (a) $\delta_1 = 0.2$, $\delta_2 = 0$ and (b) $\delta_1 = 0$, $\delta_2 = 0.25$, respectively, with insets demonstrating distribution profiles of OBC eigenstates with the same colors. [(a2),(b2)] The inverse localization length $\kappa_\pm(k)$ for the two bands marked by the same colors in (a1) and (b1). In (b2), blue and red curves overlap as $\kappa_{2,+}(k) = \kappa_{2,-}(k)$. Other parameters are $t_1 = 1$, $t_2 = 1.5$ and $N = 40$.

directions. Therefore we shall treat these two parameters separately in the following discussion.

We first give a systematic analysis of the case in the presence of a nonzero δ_1. The Bloch Hamiltonian becomes

$$h_1(k) = (t_1 + t_2 \cos k)\sigma_x + t_2 \sin k \sigma_y + i2\delta_1 \sin k \sigma_0,$$

with its eigenenergies given by

$$E_{1,\pm}(k) = i2\delta_1 \sin k \pm \sqrt{t_1^2 + t_2^2 + 2t_1 t_2 \cos k}, \quad \text{(B1)}$$

supporting the same DP as the Hermitian SSH model. Moreover, $h_1(k)$ satisfy

$$\sigma_y h_1(k)\sigma_y = -h_1^*(k), \quad \text{(B2)}$$

so that the eigenenergies of $h_1(k)$ are always symmetric about the imaginary axis (Re$E = 0$), i.e., $E_+(k) = -E_-^*(k)$, as shown in Fig. 8(a1). Therefore a real line-gap always presences between the two bands $E_{1,\pm}$ except when they touch at Re$E = 0$, avoiding the band overlapping problem.

In 1D systems, NHSE can be quantitatively described by generalizing the Bloch Hamiltonian to a non-Bloch one, $H(k) \rightarrow H(k + i\kappa(k))$, where $\kappa(k)$ describes the inverse localization length of skin modes [7,16]. The eigenenergies of Eq. (B1) satisfy

$$E_{1,+}(k + i\kappa) = -E_{1,-}^*(k - i\kappa), \quad \text{(B3)}$$

where κ is a arbitrary constant inverse localization length. Assuming the inverse localization length is given by $\kappa_\pm(k)$ for two bands, the OBC eigenenergies must have paired k and k' satisfying

$$E_\pm[k + i\kappa_\pm(k)] = E_\pm[k' + i\kappa_\pm(k)]. \quad \text{(B4)}$$

The exact relation between k and k' is unknown, yet from Eqs. (B3) and (B4) we will also have

$$E_{1,-}[k - i\kappa_{1,+}(k)] = E_{1,-}[k' - i\kappa_{1,+}(k)]. \quad \text{(B5)}$$

Combining the Eqs. (B4) and (B5), we reach the conclusion that

$$\kappa_{1,+}(k) = -\kappa_{1,-}(k), \quad \text{(B6)}$$

meaning that the eigenstates have opposite localizing directions for the two bands, as shown in the Fig. 8(a2) and the insets of Fig. 8(a1).

Similar analytics can be applied to the case in the presence of a nonzero δ_2. The Hamiltonian in momentum space is given by

$$h_2(k) = (t_1 + t_2 \cos k + i2\delta_2 \sin k)\sigma_x + t_2 \sin k\sigma_y,$$

which satisfies the chiral symmetry

$$\sigma_z h_2(k)\sigma_z = -h_2(k). \quad \text{(B7)}$$

The eigenvalues of $h_2(k)$ appear in $(E, -E)$ pairs,

$$E_{2,\pm}(k) = \pm\sqrt{(t_1 + t_2 \cos k + i2\delta_2 \sin k)^2 + (t_2 \sin k)^2}, \quad \text{(B8)}$$

as shown in Fig. 8(b1). With the non-Bloch generalization taken into account, the eigenenergies satisfies

$$E_{2,+}(k + i\kappa) = -E_{2,-}(k + i\kappa). \quad \text{(B9)}$$

Combining Eqs. (B4) and (B9) we shall obtain

$$\kappa_{2,+}(k) = \kappa_{2,-}(k), \quad \text{(B10)}$$

meaning that the eigenstates have the same localizing direction for the two bands, as shown in the Fig. 8(b2) and the insets of Fig. 8(b1).

[1] M. Z. Hasan and C. L. Kane, *Colloquium*: Topological insulators, Rev. Mod. Phys. **82**, 3045 (2010).

[2] X.-L. Qi and S.-C. Zhang, Topological insulators and superconductors, Rev. Mod. Phys. **83**, 1057 (2011).

[3] S. Ryu and Y. Hatsugai, Topological origin of zero-energy edge states in particle-hole symmetric systems, Phys. Rev. Lett. **89**, 077002 (2002).

[4] R. S. K. Mong and V. Shivamoggi, Edge states and the bulk-boundary correspondence in Dirac Hamiltonians, Phys. Rev. B **83**, 125109 (2011).

[5] A. P. Schnyder, S. Ryu, A. Furusaki, and A. W. W. Ludwig, Classification of topological insulators and superconductors in three spatial dimensions, Phys. Rev. B **78**, 195125 (2008).

[6] P. Delplace, D. Ullmo, and G. Montambaux, Zak phase and the existence of edge states in graphene, Phys. Rev. B **84**, 195452 (2011).

[7] C. H. Lee and R. Thomale, Anatomy of skin modes and topology in non-Hermitian systems, Phys. Rev. B **99**, 201103 (2019).

[8] V. M. Martinez Alvarez, J. E. Barrios Vargas, and L. E. F. Foa Torres, Non-Hermitian robust edge states in one dimension:

Anomalous localization and eigenspace condensation at exceptional points, Phys. Rev. B **97**, 121401 (2018).

[9] T. E. Lee, Anomalous edge state in a non-Hermitian lattice, Phys. Rev. Lett. **116**, 133903 (2016).

[10] F. K. Kunst, E. Edvardsson, J. C. Budich, and E. J. Bergholtz, Biorthogonal bulk-boundary correspondence in non-Hermitian systems, Phys. Rev. Lett. **121**, 026808 (2018).

[11] L. Jin and Z. Song, Bulk-boundary correspondence in a non-Hermitian system in one dimension with chiral inversion symmetry, Phys. Rev. B **99**, 081103(R) (2019).

[12] E. Edvardsson, F. K. Kunst, and E. J. Bergholtz, Non-Hermitian extensions of higher-order topological phases and their biorthogonal bulk-boundary correspondence, Phys. Rev. B **99**, 081302(R) (2019).

[13] Y. Xiong, Why does bulk boundary correspondence fail in some non-Hermitian topological models, J. Phys. Commun. **2**, 035043 (2018).

[14] R. Koch and J. C. Budich, Bulk-boundary correspondence in non-Hermitian systems: Stability analysis for generalized boundary conditions, Europhys. J. D **74**, 70 (2020).

[15] E. Edvardsson and E. Ardonne, Sensitivity of non-Hermitian systems, Phys. Rev. B **106**, 115107 (2022).

[16] S. Yao and Z. Wang, Edge states and topological invariants of non-Hermitian systems, Phys. Rev. Lett. **121**, 086803 (2018).

[17] K. Yokomizo and S. Murakami, Non-Bloch band theory of non-Hermitian systems, Phys. Rev. Lett. **123**, 066404 (2019).

[18] K. Zhang, Z. Yang, and C. Fang, Correspondence between winding numbers and skin modes in non-Hermitian systems, Phys. Rev. Lett. **125**, 126402 (2020).

[19] Z. Yang, K. Zhang, C. Fang, and J. Hu, Non-Hermitian bulk-boundary correspondence and auxiliary generalized Brillouin zone theory, Phys. Rev. Lett. **125**, 226402 (2020).

[20] C. H. Lee, L. Li, R. Thomale, and J. Gong, Unraveling non-Hermitian pumping: Emergent spectral singularities and anomalous responses, Phys. Rev. B **102**, 085151 (2020).

[21] W. P. Su, J. R. Schrieffer, and A. J. Heeger, Solitons in polyacetylene, Phys. Rev. Lett. **42**, 1698 (1979).

[22] H.-Q. Liang and L. Li, Topological properties of non-Hermitian Creutz ladders, Chin. Phys. B **31**, 010310 (2022).

[23] A. A. Mailybaev, O. N. Kirillov, and A. P. Seyranian, Geometric phase around exceptional points, Phys. Rev. A **72**, 014104 (2005).

[24] C. Yin, H. Jiang, L. Li, R. Lü, and S. Chen, Geometrical meaning of winding number and its characterization of topological phases in one-dimensional chiral non-Hermitian systems, Phys. Rev. A **97**, 052115 (2018).

[25] L. Li, C. H. Lee, and J. Gong, Geometric characterization of non-Hermitian topological systems through the singularity ring in pseudospin vector space, Phys. Rev. B **100**, 075403 (2019).

[26] D. C. Brody, Biorthogonal quantum mechanics, J. Phys. A: Math. Theor. **47**, 035305 (2014).

[27] V. Kozii and L. Fu, Non-Hermitian topological theory of finite-lifetime quasiparticles: Prediction of bulk Fermi arc due to exceptional point, arxiv:1708.05841.

[28] P. Pujol-Closa, L. Torner, and D. Artigas, Dirac points embedded in the continuum, Phys. Rev. B **108**, 205106 (2023).

[29] H. Zhou, C. Peng, Y. Yoon, C. W. Hsu, K. A. Nelson, L. Fu, J. D. Joannopoulos, M. Soljacic, and B. Zhen, Observation of bulk Fermi arc and polarization half charge from paired exceptional points, Science **359**, 1009 (2018).

[30] W. A. Benalcazar, B. A. Bernevig, and T. L. Hughes, Quantized electric multipole insulators, Science **357**, 61 (2017).

[31] Z. Song, Z. Fang, and C. Fang, $(d-2)$-dimensional edge states of rotation symmetry protected topological states, Phys. Rev. Lett. **119**, 246402 (2017).

[32] W. Jia, X.-C. Zhou, L. Zhang, L. Zhang, and X.-J. Liu, Unified characterization for higher-order topological phase transitions, Phys. Rev. Res. **5**, L022032 (2023).

[33] E. Khalaf, Higher-order topological insulators and superconductors protected by inversion symmetry, Phys. Rev. B **97**, 205136 (2018).

[34] Z. Lei, Y. Deng, and L. Li, Topological classification of higher-order topological phases with nested band inversion surfaces, Phys. Rev. B **106**, 245105 (2022).

[35] X.-W. Luo and C. Zhang, Higher-order topological corner states induced by gain and loss, Phys. Rev. Lett. **123**, 073601 (2019).

[36] C. H. Lee, L. Li, and J. Gong, Hybrid higher-order skin-topological modes in nonreciprocal systems, Phys. Rev. Lett. **123**, 016805 (2019).

[37] Y. Li, C. Liang, C. Wang, C. Lu, and Y.-C. Liu, Gain-loss-induced hybrid skin-topological effect, Phys. Rev. Lett. **128**, 223903 (2022).

[38] W. Zhu and J. Gong, Hybrid skin-topological modes without asymmetric couplings, Phys. Rev. B **106**, 035425 (2022).

[39] T. Helbig, T. Hofmann, S. Imhof, M. Abdelghany, T. Kiessling, L. W. Molenkamp, C. H. Lee, A. Szameit, M. Greiter, and R. Thomale, Generalized bulk–boundary correspondence in non-Hermitian topolectrical circuits, Nat. Phys. **16**, 747 (2020).

[40] T. Hofmann, T. Helbig, F. Schindler, N. Salgo, M. Brzezińska, M. Greiter, T. Kiessling, D. Wolf, A. Vollhardt, A. Kabaši *et al.*, Reciprocal skin effect and its realization in a topolectrical circuit, Phys. Rev. Res. **2**, 023265 (2020).

[41] D. Zou, T. Chen, W. He, J. Bao, C. H. Lee, H. Sun, and X. Zhang, Observation of hybrid higher-order skin-topological effect in non-Hermitian topolectrical circuits, Nat. Commun. **12**, 7201 (2021).

[42] W. Deng, T. Chen, and X. Zhang, *n*th power root topological phases in Hermitian and non-Hermitian systems, Phys. Rev. Res. **4**, 033109 (2022).

[43] H. Zhang, T. Chen, L. Li, C. H. Lee, and X. Zhang, Electrical circuit realization of topological switching for the non-Hermitian skin effect, Phys. Rev. B **107**, 085426 (2023).

[44] S. Weidemann, M. Kremer, T. Helbig, T. Hofmann, A. Stegmaier, M. Greiter, R. Thomale, and A. Szameit, Topological funneling of light, Science **368**, 311 (2020).

[45] L. Xiao, T. Deng, K. Wang, G. Zhu, Z. Wang, W. Yi, and P. Xue, Non-Hermitian bulk–boundary correspondence in quantum dynamics, Nat. Phys. **16**, 761 (2020).

[46] Q. Lin, T. Li, L. Xiao, K. Wang, W. Yi, and P. Xue, Topological phase transitions and mobility edges in non-Hermitian quasicrystals, Phys. Rev. Lett. **129**, 113601 (2022).

[47] Q. Lin, T. Li, L. Xiao, K. Wang, W. Yi, and P. Xue, Observation of non-Hermitian topological Anderson insulator in quantum dynamics, Nat. Commun. **13**, 3229 (2022).

[48] X. Zhang, Y. Tian, J.-H. Jiang, M.-H. Lu, and Y.-F. Chen, Observation of higher-order non-Hermitian skin effect, Nat. Commun. **12**, 5377 (2021).

[49] L. Zhang, Y. Yang, Y. Ge, Y.-J. Guan, Q. Chen, Q. Yan, F. Chen, R. Xi, Y. Li, D. Jia *et al.*, Acoustic non-Hermitian skin effect from twisted winding topology, Nat. Commun. **12**, 6297 (2021).

[50] H. Gao, H. Xue, Z. Gu, L. Li, W. Zhu, Z. Su, J. Zhu, B. Zhang, and Y. D. Chong, Anomalous Floquet non-Hermitian skin effect in a ring resonator lattice, Phys. Rev. B **106**, 134112 (2022).

[51] Z. Gu, H. Gao, H. Xue, J. Li, Z. Su, and J. Zhu, Transient non-Hermitian skin effect, Nat. Commun. **13**, 7668 (2022).

[52] W. N. Faugno and T. Ozawa, Interaction-induced non-Hermitian topological phases from a dynamical gauge field, Phys. Rev. Lett. **129**, 180401 (2022).

[53] R. Shen and C. H. Lee, Non-Hermitian skin clusters from strong interactions, Commun. Phys. **5**, 238 (2022).

[54] Y. Qin and L. Li, Occupation-dependent particle separation in one-dimensional non-Hermitian lattices, Phys. Rev. Lett. **132**, 096501 (2024).

[55] Y. Qin, K. Zhang, and L. Li, Geometry-dependent skin effect and anisotropic Bloch oscillations in a non-Hermitian optical lattice, Phys. Rev. A **109**, 023317 (2024).

[56] M. Zheng, Y. Qiao, Y. Wang, J. Cao, and S. Chen, Exact solution of the Bose-Hubbard model with unidirectional hopping, Phys. Rev. Lett. **132**, 086502 (2024).

[57] M. Atala, M. Aidelsburger, J. T. Barreiro, D. Abanin, T. Kitagawa, E. Demler, and I. Bloch, Direct measurement of the Zak phase in topological Bloch bands, Nat. Phys. **9**, 795 (2013).

[58] S. Nakajima, T. Tomita, S. Taie, T. Ichinose, H. Ozawa, L. Wang, M. Troyer, and Y. Takahashi, Topological Thouless pumping of ultracold fermions, Nat. Phys. **12**, 296 (2016).

[59] M. Lohse, C. Schweizer, O. Zilberberg, M. Aidelsburger, and I. Bloch, A Thouless quantum pump with ultracold bosonic atoms in an optical superlattice, Nat. Phys. **12**, 350 (2016).

[60] Y.-J. Lin, K. Jiménez-García, and I. B. Spielman, Spin–orbit-coupled Bose–Einstein condensates, Nature (London) **471**, 83 (2011).

[61] L. W. Cheuk, A. T. Sommer, Z. Hadzibabic, T. Yefsah, W. S. Bakr, and M. W. Zwierlein, Spin-injection spectroscopy of a spin-orbit coupled Fermi gas, Phys. Rev. Lett. **109**, 095302 (2012).

[62] Z. Wu, L. Zhang, W. Sun, X.-T. Xu, B.-Z. Wang, S.-C. Ji, Y. Deng, S. Chen, X.-J. Liu, and J.-W. Pan, Realization of two-dimensional spin-orbit coupling for Bose-Einstein condensates, Science **354**, 83 (2016).

[63] L. Huang, Z. Meng, P. Wang, P. Peng, S.-L. Zhang, L. Chen, D. Li, Q. Zhou, and J. Zhang, Experimental realization of two-dimensional synthetic spin–orbit coupling in ultracold Fermi gases, Nat. Phys. **12**, 540 (2016).

[64] M. Creutz, End states, ladder compounds, and domain-wall fermions, Phys. Rev. Lett. **83**, 2636 (1999).

[65] J. H. Kang, J. H. Han, and Y. Shin, Realization of a cross-linked chiral ladder with neutral fermions in a 1D optical lattice by orbital-momentum coupling, Phys. Rev. Lett. **121**, 150403 (2018).

[66] J. H. Kang, J. H. Han, and Y. I. Shin, Creutz ladder in a resonantly shaken 1D optical lattice, New J. Phys. **22**, 013023 (2020).

[67] J. Li, A. K. Harter, J. Liu, L. de Melo, Y. N. Joglekar, and L. Luo, Observation of parity-time symmetry breaking transitions in a dissipative Floquet system of ultracold atoms, Nat. Commun. **10**, 855 (2019).

[68] Z. Ren, D. Liu, E. Zhao, C. He, K. K. Pak, J. Li, and G.-B. Jo, Chiral control of quantum states in non-Hermitian spin–orbit-coupled fermions, Nat. Phys. **18**, 385 (2022).

[69] Q. Liang, D. Xie, Z. Dong, H. Li, H. Li, B. Gadway, W. Yi, and B. Yan, Dynamic signatures of non-Hermitian skin effect and topology in ultracold atoms, Phys. Rev. Lett. **129**, 070401 (2022).

[70] W. X. Teo, L. Li, X. Zhang, and J. Gong, Topological characterization of non-Hermitian multiband systems using Majorana's stellar representation, Phys. Rev. B **101**, 205309 (2020).